

T3D: Towards 3D Medical Image Understanding through Vision-Language Pre-training

Che Liu¹, Cheng Ouyang¹, Yinda Chen⁵, César Quilodrán-Casas¹, Lei Ma⁴,
Jie Fu², Yike Guo², Anand Shah^{1,3}, Wenjia Bai¹, Rossella Arcucci¹

¹Imperial College London

²Hong Kong University of Science and Technology

³Royal Brompton and Harefield Hospital

⁴Peking University

⁵University of Science and Technology of China

Abstract

Expert annotation of 3D medical image for downstream analysis is resource-intensive, posing challenges in clinical applications. Visual self-supervised learning (vSSL), though effective for learning visual invariance, neglects the incorporation of domain knowledge from medicine. To incorporate medical knowledge into visual representation learning, vision-language pre-training (VLP) has shown promising results in 2D image. However, existing VLP approaches become generally impractical when applied to high-resolution 3D medical images due to GPU hardware constraints and the potential loss of critical details caused by downsampling, which is the intuitive solution to hardware constraints. To address the above limitations, we introduce T3D, the first VLP framework designed for high-resolution 3D medical images. T3D incorporates two text-informed pretext tasks: (i) text-informed contrastive learning; (ii) text-informed image restoration. These tasks focus on learning 3D visual representations from high-resolution 3D medical images and integrating clinical knowledge from radiology reports, without distorting information through forced alignment of downsampled volumes with detailed anatomical text. Trained on a newly curated large-scale dataset of 3D medical images and radiology reports, T3D significantly outperforms current vSSL methods in tasks like organ and tumor segmentation, as well as disease classification. This underlines T3D’s potential in representation learning for 3D medical image analysis. All data and code will be available upon acceptance.

1. Introduction

Deep learning (DL) has revolutionized the field of 3D medical image analysis, enhancing diagnostic accuracy and clinical efficiency, however, supervised DL methods rely

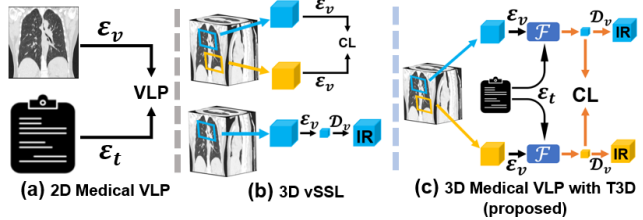


Figure 1. (a) Conventional 2D VLP framework. (b) **Top**: Framework of vSSL with contrastive learning. (b) **Bottom**: Framework of vSSL with image restoration. (c) The concept of **T3D (ours)**. T3D is designed specifically for 3D visual representation learning from both clinical reports and 3D medical images. \mathcal{E}_v represents the visual encoder, while \mathcal{D}_v denotes the visual decoder. \mathcal{F} serves as the interactor, aiming to make visual features informed by text features.

on high-quality annotations which is laborious and costly. To minimize the reliance on manual labelling, visual self-supervised learning (vSSL) shows remarkable progress in capitalizing on the vast reservoir of unlabeled medical data. Existing vSSL techniques include image restoration and contrastive learning [3, 12, 14, 33, 36, 44]. Image restoration (IR) focuses on reconstructing the original image from its corrupted counterpart [6, 12, 15, 29, 36, 41, 45], while contrastive learning (CL) emphasizes distinguishing between positive and negative samples [3, 14, 21, 33, 44]. However, these methods face two primary hurdles:

Insufficient High-level Semantics from IR: The IR-based vSSL methods predominantly concentrate on restoring original images through low-level semantics, leaving high-level semantics substantially overlooked, as discussed in [15, 27, 28]. Nonetheless, high-level semantics play a pivotal role in downstream image analysis tasks, such as disease classification and tumour segmentation. The absence of high-level semantics could, therefore, hinder the efficacy of pre-trained models for downstream tasks.

Semantic Misalignment in Positive/Negative Pairs Construction in Patch-based CL: Recent advancements in CL-based vSSL methods for 3D medical imaging often take two distinct 3D patches from the *same* image to form *positive* pairs in a CL framework (*i.e.*, to enforce their features to be the same) [13, 34, 52]. However, these positive patches, enforced to align in CL, may originate from distinct anatomical regions and not share similar semantics [21]. Meanwhile, *negative* pairs (*i.e.*, intended to have different features) might come from similar anatomical regions. This can lead to semantic misalignment due to the conflicting relationships between positive/negative pairs and their anatomical relevance, potentially obstructing the ability of the pre-trained model to learn discriminative 3D visual features.

Vision-Language Pre-training (VLP) has emerged as a promising approach to tackle these challenges [25, 26, 31, 50]. VLP enhances the learning of clinically relevant and semantically enriched representations by aligning medical images with their corresponding radiology reports. In this process, the improved feature informativeness is achieved with the additional supervision provided by the radiology reports [18]. This pretext task shows potential to significantly improve model performance across a variety of 2D medical image tasks, as evidenced by [24, 37, 38, 49, 50]. However, despite the proven effectiveness of VLP in 2D medical imaging, its applicability and potential benefits for 3D medical images remain largely underexplored: Due to the GPU hardware limitations, in VLP, the model can only process cropped local sub-volumes of an entire 3D medical image [14, 21, 34, 44], leading to a mismatch between local-level visual features from the cropped patch and the global-level medical reports associated with the entire volume. Although downsampling techniques [23, 43] can reduce the computational burden associated with processing entire high-resolution volumes in VLP, it inevitably loses information in resolution decreasing, potentially affecting downstream tasks that rely on subtle local information, such as tumour segmentation. Besides the aforementioned issues, there is a substantial shortage of publicly accessible datasets for developing and testing **3D** medical VLP approaches.

To address these challenges, the contributions of our work are three-fold:

1. We introduce T3D, a novel VLP framework tailored for 3D medical image analysis. It innovatively (i) leverages text information from clinical reports to construct positive and negative pairs for the contrastive learning pretext task, thus mitigating the biases inherent in vSSL methods that align augmented views of arbitrarily cropped sub-volumes; and (ii) further exploits text information to guide the image restoration pretext task with corrupted sub-volumes, thereby enhancing visual repre-

sentation learning.

2. To facilitate the research community for developing and assessing 3D medical VLP, we curate the first **publicly accessible** dataset that includes 3D medical image-report pairs, based on public data sources and with assistance from expert radiologists. Additionally, we provide the first large-scale multi-label classification dataset with 3D medical images, covering around 100 diseases, to evaluate the quality of the learned visual representation from 3D VLP methods.
3. For the first time, we showcase the efficacy of VLP in 3D medical image analysis using T3D across four distinct 3D medical imaging tasks, underscoring the versatility and robustness of the representations learned by T3D.

2. Related Work

2.1. VLP in Medical Imaging

VLP for 2D Medical Images In the realm of 2D medical images, VLP has been explored in bridging visual and textual modalities. Early efforts, such as ConVIRT [50], aimed to align images with their textual descriptions globally. This approach was refined by GLoRIA and MGCA [18, 38], which emphasized both global and local image-report alignments. While these methods enriched cross-modal representation learning, they occasionally faced challenges with token-level misalignments. Some VLP techniques, like Med-UniC [37], focused on neutralizing language biases, while others, such as MedKLIP [42] and KAD [49], leveraged domain-specific knowledge from external datasets. However, reliance on external resources posed potential generalizability concerns. On the reconstruction front, methods like MRM [51] and PRIOR [11] utilized image and text token reconstruction as a pretext task. An advanced version of this approach was introduced by [19], which adjusted token weights during the reconstruction phase, enhancing the quality of learned representations.

However, while these methods have shown promise in the 2D medical image domain, their direct application to 3D medical images is not straightforward. The inherent complexities of 3D volumetric data, such as the added depth dimension, and coronal spatial relationships, pose unique challenges. Additionally, aligning high-resolution 3D volumes with medical reports as a unified entity, following the protocols of 2D medical VLP, proves challenging. This difficulty arises primarily because current GPUs struggle to process such large inputs—for instance, a single 3D volume with dimensions of $512 \times 512 \times 256$ [39, 40]. While downsampling offers a potential solution, it unfortunately results in the loss of subtle information. Despite recent works [13, 21, 34] employing cropped 3D patches as inputs to preserve information from high-resolution images, a mis-

This curation protocol will be released upon acceptance.

alignment issue persists. The textual descriptions in medical reports typically correspond to the entire 3D volume, leading to discrepancies between the cropped sub-volumes and the medical reports. As a result, specialized methodologies tailored for 3D medical images are imperative for effective VLP in this domain.

VLP for 3D Medical Images Transitioning from 2D to 3D vision, while there have been developments in non-medical domains [8, 30, 46–48], these are hardly transferable to 3D medical images. This is primarily because they are specifically designed for 3D point cloud data, which is sparse, whereas 3D medical images, such as computerized tomography (CT) scans, are typically dense. The emerging field of 3D medical VLP has begun to address this issue, albeit with various challenges. From a methodological perspective, works such as [7, 9] opt to align entire medical reports with cropped sub-volumes directly. This method introduces mismatch biases, as it aligns a local patch with a report describing the entire volume. Conversely, [23, 43] attempt to alleviate the bias issue by downsampling high-resolution 3D volumes to a lower resolution, allowing alignment with the complete medical report but at the cost of losing detailed information inherent in high-resolution volumes. This downsampling not only diminishes the richness of the data but also limits the input size for tasks like segmentation, potentially affecting the granularity and accuracy of the results. Moreover, the use of non-publicly accessible data for training by [43] and [23] places additional burdens on the research community, limiting reproducibility and the broader application of their findings.

In essence, these initial forays into applying VLP to 3D medical images, while noteworthy, do not harness the information contained within high-resolution 3D volumes, frequently resulting in biases of misalignment or the omission of subtle details throughout the process. There is a distinct need for methodologies that can more adeptly alleviate these challenges.

2.2. Visual SSL in 3D Medical Imaging

Restoration-based Methods vSSL employs image restoration (IR) techniques to learn visual features by reconstructing corrupted images to their original state. While significant progress has been made for photographic images [6, 12, 15, 29, 36, 41, 45], adaptations for medical images often don’t fully address its unique challenges. For instance, [5] focused on global representation through masked voxel restoration but lacked depth in slice-level and local representations. [54] leveraged recurrent anatomical patterns in 3D medical images for vSSL, eliminating the need for manual annotations. And while [10, 53] delved into masked image modeling for 3D medical image analysis, the comprehensive semantic understanding of both global and local representations remains underexplored,

as IR primarily hinges on low-level visual semantics [15, 27, 28].

Alignment-based Methods Contrastive learning (CL), which primarily relies on aligning positive samples, has seen applications in medical imaging [3, 14, 33, 44]. These studies often treat different sub-volumes from the same volume as positive pairs. However, the local bias introduced by constructing positive pairs from homologous sub-volumes is highlighted by [21]. While recent efforts [21, 34, 52, 55] have attempted to combine CL and IR as pretext tasks for 3D medical image vSSL, challenges remain in addressing biases from positive pair construction and in extracting high-level semantics from IR. The recent work, vox2vec [13], presents a fine-grained CL approach using voxel alignment from sub-volume. However, its effectiveness in learning representative features might be constrained since neighboring voxels, typically originating from the same tissue, are often correlated, yet [13] treats them as negative samples. This approach also faces the bias associated with sub-volume cropping, as discussed in [21].

These efforts constitute important steps toward better vSSL methods for 3D medical image analysis. Nevertheless, Our work distinguishes itself by having two crucial new developments: (1) the incorporation of clinical reports as a supervised signal, utilizing their expert-verified clinical domain knowledge, and (2) The alleviation of local bias in the construction of contrastive pairs, achieved through our novel approach of text-informed positive pair construction.

3. Methodology

The proposed T3D framework aims to learn both clinical knowledge and visual representation from high-resolution 3D medical images and their accompanied medical reports. The T3D consists of two text-driven pretext tasks: (i) Text-informed Image Restoration (TIR) and (ii) Text-informed Contrastive Learning (TCL).

3.1. Framework

Our framework utilizes an encoder-decoder structure as its visual backbone and incorporates a BERT-based model for text encoding, as shown in Fig 2. Given a training dataset \mathcal{X} comprised of N 3D image-text pairs, we present each pair as (i_q, t_q) , where $i_q \in \mathcal{I}$ signifies the raw three-dimensional image and $t_q \in \mathcal{T}$ signifies the associated text report, respectively, and $q = 1, 2, 3, \dots, N$.

To maintain the rich detailed information inherent in high-resolution 3D medical images, we avoid downsamplings and instead perform random croppings to obtain two 3D sub-volumes from the same entire volume, as illustrated in the left part of Fig 2. These sub-volumes are denoted as (i_q^1, i_q^2) , where $i_q^1, i_q^2 \in \mathbb{R}^{1 \times H \times W \times D}$. Consequently, the sub-volumes-to-report pairing can be described as (i_q^1, i_q^2, t_q) .

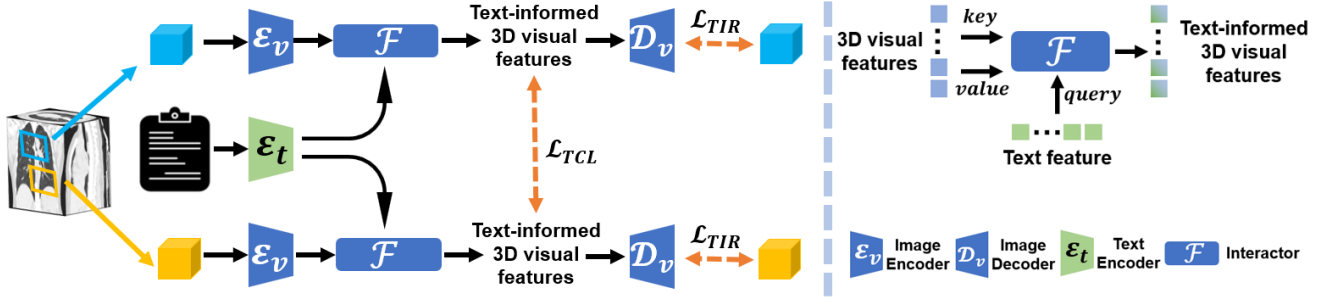


Figure 2. **Left:** Framework of T3D. We crop two 3D sub-volumes, apply data augmentation, and process them through a visual encoder for their visual features. Concurrently, a text encoder extracts features from the corresponding clinical report. These visual features, after being informed by textual data via the interactor module (right figure), are used as positive pairs for alignment and for image restoration, enhancing visual representation learning. **Right:** Structure of the Interactor. Here, 3D visual features serve as *key* and *value*, with text features as *query* in attention of this transformer-based block. Post attention mechanism, these visual features are text-informed.

As illustrated in Fig 2, the visual encoder, \mathcal{E}_v , serves to convert the sub-volume into embeddings with dimensions $(C, \frac{H}{16}, \frac{W}{16}, \frac{D}{16})$, where C denotes the number of channels. The text encoder, \mathcal{E}_t , transforms the text report into embeddings of dimension (L, R) . In this case, L represents the length of the input text token sequence, and R is the dimension of the text token embedding. To ensure compatibility for subsequent fusion procedures, we maintain $R = C$, which allows the dimension of the text embedding to be expressed as (L, C) .

The visual and textual features can be obtained as:

$$\mathbf{i}_q^1 = \mathcal{E}_v(i_q^1), \mathbf{i}_q^2 = \mathcal{E}_v(i_q^2), \mathbf{t}_q = \mathcal{E}_t(t_q)$$

where $(\mathbf{i}_q^1, \mathbf{i}_q^2)$ are visual features, and \mathbf{t}_q is the text feature. Hence, the dataset in feature-level, \mathbf{D} , can then be represented as:

$$\mathbf{D} = \{(\mathbf{i}_1^1, \mathbf{i}_1^2, \mathbf{t}_1), (\mathbf{i}_2^1, \mathbf{i}_2^2, \mathbf{t}_2), \dots, (\mathbf{i}_N^1, \mathbf{i}_N^2, \mathbf{t}_N)\}$$

Subsequently, to facilitate the interaction between visual and textual features, we propose a transformer-based block module, termed as *interactor* and denoted as $\mathcal{F}(\cdot)$, as shown in Fig 2. The interactor module integrates textual information into visual features through an attention mechanism, using both as inputs. Specifically, as shown in the right part of Fig 2, the architecture of this interactor comprises a single transformer decoder layer. The visual features are then set as the *key* and *value* in attention, while the text feature serves as the *query*. As a result, the output of $\mathcal{F}(\cdot)$, which represents the text-informed visual features $\mathbf{i}_q^{1,\text{info}}$ and $\mathbf{i}_q^{2,\text{info}}$, is calculated as:

$$\begin{aligned} \mathbf{i}_q^{1,\text{info}} &= \mathcal{F}(\mathbf{t}_q, \mathbf{i}_q^1) \\ \mathbf{i}_q^{2,\text{info}} &= \mathcal{F}(\mathbf{t}_q, \mathbf{i}_q^2) \end{aligned} \quad (1)$$

We ablate the specific number of layers and attention heads in Sec 4.6.3.

3.2. Text-informed Contrastive Learning

After deriving the text-informed visual features of two sub-volumes from the same CT scan, we construct a positive pair using these features. We then consider the sub-volumes from other CT scans as negative samples. To apply the contrastive loss, we implement 3D average pooling on the text-informed visual features. Following this, we project the pooled features to a 128-dimensional space using two distinct non-linear projectors, denoted as $(\mathcal{P}^1, \mathcal{P}^2)$, for each sub-volume feature. Hence, the loss function of *text-informed contrastive learning* (TCL) is described by:

$$\mathcal{L}_{\text{TCL}} = -\log \frac{\exp(s_{q,q}/\sigma)}{\sum_{j=1}^K \exp(s_{q,j}/\sigma)},$$

$$\text{where } s_{q,q} = \hat{\mathbf{i}}_q^{1,\text{info}\top} \cdot \hat{\mathbf{i}}_q^{2,\text{info}}, \quad (2)$$

$$\hat{\mathbf{i}}_q^{1,\text{info}} = \mathcal{P}^1(\text{Avgpool}(\mathbf{i}_q^{1,\text{info}})),$$

$$\hat{\mathbf{i}}_q^{2,\text{info}} = \mathcal{P}^2(\text{Avgpool}(\mathbf{i}_q^{2,\text{info}})),$$

and σ is the temperature factor set as 0.07 following [31].

3.3. Text-informed Image Restoration

To enhance the visual feature learning with text reports, we introduced an auxiliary pretext task: *text-information image restoration* (TIR) to enhance the visual representation learning. This task aims to restore the corrupted volume using text-informed visual features. The training objective for this task can be formulated as:

$$\begin{aligned} \mathcal{L}_{\text{TIR}} &= (\|i_q^1 - \hat{i}_q^1\|_1 + \|i_q^2 - \hat{i}_q^2\|_1) \\ \text{where } \hat{i}_q^1 &= \mathcal{D}_v(\mathbf{i}_q^{1,\text{info}}), \hat{i}_q^2 = \mathcal{D}_v(\mathbf{i}_q^{2,\text{info}}) \end{aligned} \quad (3)$$

Overall Training Objective With a synergy of TCL and TIR, the overall pre-training objective of our T3D framework can be represented as follows:

$$\mathcal{L}_{\text{total}} = \mathcal{L}_{\text{TCL}} + \mathcal{L}_{\text{TIR}}. \quad (4)$$

<https://pytorch.org/docs/stable/generated/torch.nn.Transformer.html>

<https://pytorch.org/docs/stable/generated/torch.nn.AvgPool3d.html>

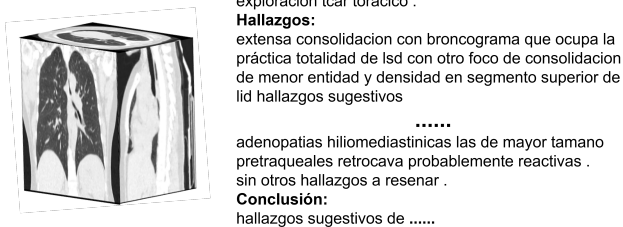


Figure 3. An exemplar of 3D CT scan and paired radiology report from our curated BIMCV-VLP dataset.

After pre-training, the obtained image encoder can be used as a strong pre-training visual backbone for downstream task-specific fine-tuning.

4. Experiments

In the experimental section, we evaluate our method against recent SOTA 3D medical vSSL methods. For detailed implementation specifics and dataset descriptions, please refer to the appendix due to space limitations in the main text.

4.1. Pre-training Dataset

BIMCV-VLP For this work, we utilized the BIMCV [35] dataset as the foundation for creating our 3D medical VLP dataset. Originating from Valencia, Spain, the BIMCV dataset [35] provides raw CT scans, radiology reports, and DICOM metadata.

To curate the pre-training dataset, we followed these steps:

1. Filtered out samples that either lacked a report or has a report shorter than 5 words.
2. Excluded samples that has a report but no associated available CT scans.
3. Removed samples with reports where the CT scans has dimensions (width, height, or depth) smaller than 96 on any axis.

After implementing the above steps, we curated a dataset specifically for training T3D, consisting of 8,069 samples. We visualize a 3D scan and associated report in Fig 3. Each sample in this dataset pairs a CT image with a report. We have named this dataset BIMCV-VLP. The basic statistics of BIMCV-VLP dataset is depicted as Tab 1. More visualizations of the dataset can be found in the appendix.

	Average	Median	Min	Max
Image Width	529	512	514	710
Image Height	528	512	520	672
Number of Slice	279	224	101	670
Length of Report	104	97	7	260

Table 1. Details of BIMCV-VLP dataset. The length of the report is counted by the number of words in each report.

This dataset will be released upon acceptance.

4.2. Downstream Tasks and Evaluation Metrics

In our downstream tasks, we aim to assess the effectiveness of our method across a diverse set of 3D medical imaging tasks, varying in size, objectives, and modalities. Specifically, we evaluate the representativity and adaptability of the 3D visual features informed by medical reports. These evaluations span four distinct 3D medical image tasks, covering over 100 diseases, encompassing 15 organs, and spanning both CT and magnetic resonance imaging (MRI) modalities.

Multi-organ Segmentation We implement this task using the BTCV dataset [22]. This dataset consists of 30 abdominal CT scans, each pixel-level annotated for 13 organs by radiologists from Vanderbilt University Medical Center. Following the protocols in [13], we employ a five-fold cross-validation, distributing the dataset into 70%, 10%, and 20% for training, validation, and testing, respectively. The 20% test data does not overlap with other folds. The results are presented as the average Dice score accompanied by its standard deviation across all folds. To maintain consistency in comparison, we adhere to the fine-tuning procedure outlined in [34].

Lung Tumour Segmentation For lung tumour segmentation, we utilize the Medical Segmentation Decathlon (MSD) dataset [1], comprising 63 CT scans annotated at the pixel level for lung tumours. Following the data split in [13], we conduct a three-fold cross-validation, partitioning the dataset into 70%, 10%, and 20% for training, validation, and testing, respectively. The 20% test data has no overlap with the other folds and is covered entirely across three folds. Our results include the average Dice score and its standard deviation. For a fair comparison, we also follow the fine-tuning methodology from [34].

Multi-disease Classification For the multi-disease classification task, we utilize 1,475 samples based on [35]. These samples comprise 3D CT scans accompanied by annotations for multiple diseases. It’s noteworthy that each scan might be annotated with multiple diseases, with a total of 96 distinct diseases. We employ this dataset to assess the quality of visual representations learned from pre-training and name it the Multi-Disease Long Tail Classification (MDLT) dataset. The label distribution of the MDLT dataset is shown in the appendix. In this task, we fine-tune a pre-trained visual encoder with a random initialized linear classifier. We allocate 70%, 10%, and 20% of the dataset for training, validation, and testing purposes, respectively. Our results are presented in terms of the macro-average AUC score spanning all diseases. All experiments are executed five times, each with a unique random seed.

Transfer Learning across Domains and Tasks To ex-

<https://github.com/Project-MONAI/research-contributions/tree/main/SwinUNETR/BTCV>

This dataset will be released upon acceptance

plore the transferability on different imaging modality (CT to MRI) of the 3D visual features derived from T3D, we evaluate brain tumour segmentation on the BraTS18 dataset [2] following [52, 54]. Notably, this dataset exclusively contains 277 brain MRI images, contrasting with our pre-training dataset of CT modality. BraTS18 [2] includes three categories: whole tumour (WT), tumour core (TC), and enhancing tumour (ET). We use the official data split from PCRLv2 [52] and employ the Dice score as our evaluation metric. For consistent comparisons, we adhere to the fine-tuning protocol provided by PCRLv2 [52]. We execute it with five unique random seeds and report the average results along with the standard deviation.

For all downstream tasks, we meticulously fine-tune using 1%, 10%, 20%, 100% of the training data. When the dataset contains fewer than 100 samples, we use only one sample for the 1% data fine-tuning, respectively. Detailed information, including implementation specifics, can be found in the appendix.

4.3. Implementation

Pre-training Setup We implemented T3D using PyTorch and MONAI. In T3D, the SwinUNTER[34] serves as the visual encoder and the RadBERT [4] as the text encoder, with a crop size set to $96 \times 96 \times 96$, consistent with the original SwinUNTER paper[34]. Furthermore, we freeze the text encoder to compel the visual backbone to learn more representative features. The medical report is in Spanish, but the text encoder has been pre-trained on a corpus dominated by English. To address this, we expand the vocabulary and further train the text encoder using mask language modeling, as described in [37]. During VLP, we employed a batch size of 4 on each GPU and utilized the Adam optimizer, setting a weight decay of 1×10^{-8} and an initial learning rate of 2×10^{-5} . The training is set as 50k steps, with a cosine annealing scheduler for learning rate adjustment. All pre-training experiments are implemented on 16 NVIDIA A100 GPUs.

4.4. Results on 3D Medical Image Segmentation

Multi-organ Segmentation Tab 2 showcases the results for multi-organ segmentation on the BTCV dataset [22] that includes 13 different organs. Our T3D method consistently outperforms other vSSL methods across all training data percentages. This is particularly evident in scenarios with limited training data, highlighting the robustness and adaptability of our approach.

Lung Tumour Segmentation The results from Tab 3 for lung tumour segmentation, a critical task for early cancer detection and treatment planning, further emphasize

<https://github.com/RL4M/PCRLv2>
<https://pytorch.org/>
<https://monai.io>

Multi-organ Segmentation				
Methodology	1%	10%	20%	100%
Random Init	30.1±4.6	43.1±5.1	52.6±4.9	77.0±2.5
nn-UNet3D	30.6±6.2	42.2±4.7	51.9±6.2	77.5±3.4
Patch Swapping [5]	31.2±6.3	43.5±5.2	52.2±5.4	77.4±3.1
Model Genesis [54]	30.9±5.1	43.7±4.9	52.5±5.0	77.7±3.0
MIM [10]	31.7±5.4	44.0±5.3	52.7±5.5	78.2±3.2
PCRLv2 [52]	31.8±5.0	43.6±6.1	53.1±5.1	78.1±2.9
medical MAE [53]	31.5±5.2	44.2±5.0	53.5±5.3	78.3±3.3
Tang et al [34]	32.3±4.9	44.4±4.7	54.2±4.9	78.4±2.8
vox2vec [13]	31.9±5.5	44.3±5.4	54.3±5.6	78.6±3.4
Ours	33.9±4.5	47.2±5.1	56.8±4.2	79.5±2.7

Table 2. Multi-organ segmentation results; best results bolded.

the superiority of T3D. Despite the complexities associated with lung tumour structures in the MSD dataset [1], T3D achieves the highest Dice scores across all training data ratios, underscoring its efficacy.

Lung Tumour Segmentation				
Methodology	1%	10%	20%	100%
Random Init	40.8±8.3	46.3±8.9	49.4±10.3	56.7±7.6
nn-UNet3D	43.0±5.4	46.7±5.5	49.5±7.9	55.4±12.6
Patch Swapping [5]	43.4±8.1	47.5±8.5	50.3±7.8	56.6±9.3
Model Genesis [54]	43.8±7.6	48.0±6.4	50.8±10.2	56.9±8.5
MIM [10]	44.2±6.1	48.7±8.6	51.2±9.1	57.2±8.2
PCRLv2 [52]	44.1±6.9	49.2±5.5	51.4±9.6	57.5±7.4
medical MAE [53]	44.7±4.6	49.6±6.2	51.8±7.3	57.1±8.4
Tang et al [34]	45.4±4.7	50.1±7.9	52.3±6.9	58.6±6.2
vox2vec [13]	45.6±6.9	50.4±9.3	52.0±9.0	58.4±6.4
Ours	50.1±4.2	52.4±4.9	53.2±7.0	63.6±4.1

Table 3. Lung tumor segmentation results; best results bolded.

Brain Tumour Segmentation The brain tumor segmentation results, as shown in Tab 4, highlight T3D’s impressive transferability across different imaging modalities (CT to MRI). Despite changing from CT to MRI and from chest to brain imaging, T3D excels in segmenting whole tumors (WT), tumor cores (TC), and enhancing tumors (ET). This demonstrates its adaptability across varied modalities and anatomical structures. Although T3D and other vSSL baselines are pre-trained on chest CT images, T3D incorporates clinical knowledge during this stage. The learned 3D visual features in T3D significantly boost its performance in the unseen domain and organ. We postulate that T3D’s text-informed contrastive learning helps mitigate semantic misalignment from inappropriate positive/negative pair construction in vSSL. This is because our positive/negative pairs are informed by their associated radiology reports: positive pairs share the same report, while negative pairs have different reports.

Methodology	1%				10%				20%				100%			
	Mean	WT	TC	ET	Mean	WT	TC	ET	Mean	WT	TC	ET	Mean	WT	TC	ET
Random Init	50.5±5.4	52.1	51.0	48.4	66.6±6.2	71.2	66.7	62.1	72.7±4.5	78.5	74.3	65.5	81.5±4.7	86.8	82.8	75.1
nn-UNet3D	52.1±5.5	55.9	51.2	49.2	68.3±5.8	69.6	70.7	64.7	73.6±4.9	78.6	75.2	67.1	82.3±6.0	84.4	85.4	77.2
Patch Swapping [5]	51.8±5.0	52.2	52.8	50.4	69.9±5.8	71.7	72.3	65.7	75.6±5.4	80.2	76.3	70.4	81.9±6.2	85.9	84.2	75.8
Model Genesis [54]	52.3±6.1	54.3	52.0	50.5	70.2±5.6	72.6	72.0	66.2	75.8±7.1	80.7	77.5	69.3	83.1±6.7	87.7	84.2	77.4
MIM [10]	52.8±5.5	53.7	53.1	51.8	71.6±7.2	73.5	74.4	66.8	77.3±5.4	81.8	77.2	72.8	84.3±5.8	88.1	84.4	80.6
PCRLv2 [52]	53.2±4.7	54.5	53.7	51.4	73.7±5.6	78.1	75.1	68.0	80.1±6.3	83.9	81.2	75.3	86.2±5.9	90.0	86.4	82.2
medical MAE [53]	53.3±6.5	54.4	53.5	51.9	73.6±4.4	77.7	76.2	66.8	78.8±4.6	82.6	80.5	73.4	85.4±7.0	89.2	85.7	81.4
Tang et al [34]	53.7±5.7	54.7	54.1	52.3	73.7±5.4	78.2	76.3	66.6	79.3±6.2	83.1	81.3	73.6	85.4±6.1	89.7	85.5	81.1
vox2vec [13]	53.9±4.1	54.6	54.3	52.9	74.0±4.7	78.4	76.6	67.1	79.6±5.0	83.4	81.5	73.9	85.6±4.2	90.0	85.2	81.8
Ours	56.2±3.5	57.2	56.7	54.8	76.7±3.4	79.6	79.2	71.4	80.9±3.7	84.7	82.9	75.3	87.7±4.0	91.5	87.1	84.6

Table 4. Brain Tumor Segmentation with WT (Whole Tumor), TC (Tumor Core), ET (Enhancing Tumor); best results bolded.

4.5. Results on 3D Medical Image Multi-disease Classification

The results of multi-label classification are detailed in Tab 5, elucidate the proficiency of our proposed method in multi-disease identification. The MDLT dataset, encompassing diverse 3D medical images, showcases the challenge of discerning multiple diseases. Nevertheless, our approach consistently outshines in recognizing various pathological conditions, securing the highest macro-average AUC scores across all dataset percentages. Across all tasks, T3D consistently outperforms other vSSL methods, regardless of the fine-tuning data ratio and imaging modality. This superiority can be attributed to the inherent advantages of VLP. Unlike vSSL, which primarily learns visual invariance from augmented views, VLP leverages the rich clinical knowledge encoded in text, providing a more informed supervision signal. Furthermore, the fact that T3D, pre-trained on chest CT images, achieves remarkable performance on both CT-based tasks and MRI-based brain tasks demonstrates the generalizability and transferability of the 3D visual features informed by clinical reports. This illustrates that VLP, guided by medical reports, offers more representative and transferable 3D visual features compared to vSSL.

Methodology	Multi-disease classification			
	1%	10%	20%	100%
Random Init	47.5±5.6	50.2±5.3	51.8±4.4	53.4±4.6
Patch Swapping [5]	47.9±4.9	50.5±5.2	52.0±4.3	54.1±4.5
Model Genesis [54]	48.2±4.1	51.2±4.5	53.2±3.8	53.9±5.1
MIM [10]	48.0±5.2	51.3±4.9	53.0±4.3	53.6±4.0
PCRLv2 [52]	50.5±4.6	51.6±3.9	53.6±4.0	54.0±3.7
medical MAE [53]	49.1±4.4	52.0±3.8	54.2±4.0	54.6±3.5
Tang et al [34]	50.5±3.9	52.2±4.1	54.1±4.3	56.3±3.4
vox2vec [13]	50.3±3.8	52.4±4.2	53.9±3.9	56.0±3.6
Ours	51.4±4.2	53.9±4.5	55.1±3.9	58.1±3.3

Table 5. Performance on multi-disease classification (on MDLT dataset). The metric is macro-average AUC score across all diseases. Best results are bolded.

Image Preprocessing		Alignment Strategy		Downstream Tasks	
Crop	Downsample	CLIP [31]	T3D	Brain Tumour	Lung Tumour
✓		✓		75.3±7.2	52.6±5.5
	✓	✓		76.1±6.8	52.9±6.4
	✓		✓	77.4±5.9	53.6±5.8
✓			✓	87.7±4.0	63.6±4.1

Table 6. Ablation of alignment and preprocessing strategy. The best results are bolded. ‘CLIP’ indicates that the image-report pair is aligned following the CLIP [31] strategy.

4.6. Ablation Studies

4.6.1 Impact of Alignment and Preprocessing Strategy

Tab 6 presents the ablation study on the alignment and preprocessing strategy. Initially, we utilize the alignment strategy following the CLIP-style [31], where one image-report pair is treated as a positive sample, while all other sample pairs are considered negative. For the ‘crop’ preprocessing, we utilize the random crop method, as in T3D, to produce the sub-volume to align with reports. Conversely, due to current hardware memory limitations, we downsample the entire volume from its original dimensions to $96 \times 96 \times 96$ to align the entire volume with its corresponding report. Both preprocessing techniques, when paired with the CLIP-style alignment approach, led to a notable decline in performance. This drop can be attributed to the alignment of a cropped sub-volume (offering local information) with a report that offers global information, resulting in the mismatch. Moreover, reducing the volume’s resolution leads to information loss, complicating the extraction of subtle visual features present in high-resolution images. Also, for downstream segmentation tasks that use high-resolution sub-volumes as input (because the tumour might be tiny), there’s a performance gap when transitioning from a downsampled volume during VLP to high resolution in downstream tasks.

Additionally, we apply the downsampled volume to T3D, meaning the positive pair is built on the augmented entire volume. The outcomes exhibit a minor improvement in performance compared to the CLIP-style alignment, signifying that T3D is superior to the CLIP-style method.

Ultimately, when using cropped sub-volumes from high-resolution 3D volumes and aligning them via the T3D approach, we achieved the highest performance. This highlights the critical role of retaining the initial high resolution and context for effectively learning representative and transferable 3D visual features.

4.6.2 Impact of Text driven pretext Task

In Tab 7a, we examine the effect of the text used within the interactor. We find that incorporating clinical reports into the learning process consistently enhances performance across various tasks. The informative clinical knowledge from clinical reports offers a more valuable signal compared to traditional vSSL methods, which depend only on visual invariance from augmented or masked views.

4.6.3 Ablation of Components and Hyperparameters

Text Encoder Tab 7b shows an ablation study where RadBERT [4] is replaced with ClinicalBERT [17], pre-trained on general clinical notes. The results reveal a slight performance drop with ClinicalBERT, suggesting the superiority of radiology-specific language models for 3D medical VLP.

Image Backbone To assess the versatility of our method, we employ two distinct backbones: the CNN-based U-Net [32] and the transformer-based SwinUNTER [34]. As shown in Tab 7c, the performance differences between these backbones are marginal, underscoring that our method is agnostic to the choice of backbone.

Number of Attention Heads in Interactor We conducted an ablation study on the number of attention heads in the interactor module. As depicted in Tab 7d, utilizing two attention heads produces the optimal results, with performance diminishing as the number increases to four heads. Consequently, we chose to employ two attention heads for our method.

Loss Ablation We further investigate the influence of different losses during 3D medical VLP. As depicted in Tab 7e, excluding either \mathcal{L}_{TIR} or \mathcal{L}_{TCL} leads to reduced performance. Yet, when both losses are combined, as in our method, we achieve the best results. This underscores the importance of both losses for enhancing the effectiveness of the proposed method.

Number of Transformer Layers In T3D, we utilize the transformer decoder layer to construct the interactor module. The effects of varying the number of layers are detailed in Tab 7f. The findings indicate a decline in performance as the number of transformer layers increases. The optimal results are achieved with a single Transformer layer. This suggests that a lightweight module is sufficient for integrating visual features and clinical knowledge.

4.7. Qualitative Results

Fig 4 shows the qualitative results and demonstrates the superiority of T3D. Compared with the SOTA baseline,

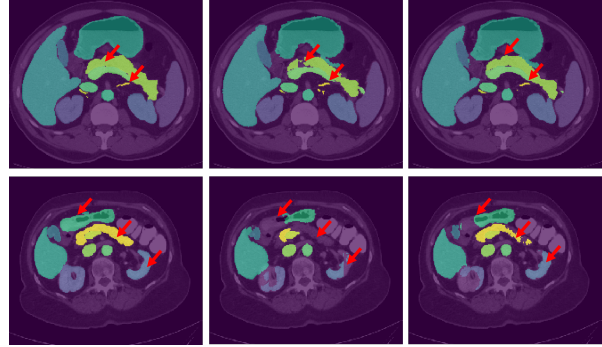


Figure 4. Qualitative visualizations on the test set from multi-organ segmentation task. **Left:** Ground truth. **Middle:** vox2vec [13], **Right:** T3D (ours).

vox2vec [13], T3D produces sharper boundaries and generates results that are more consistent with the ground truth. This success stems from the clinical knowledge from radiology reports, enhancing the 3D visual representation learning.

5. Discussion and Conclusion

While our T3D model outperform existing vSSL baselines on diverse 3D medical imaging tasks, it confronts GPU memory constraints. These limitations hinder the model’s ability to handle entire full-resolution CT scans, crucial for tasks like zero-shot classification and visual grounding that require global visual-textual alignment. Additionally, extracting text features is complicated due to the presence of abbreviations in clinical reports.

Despite these challenges, T3D stands as the first 3D medical VLP framework, adept at integrating clinical knowledge from high-resolution CT scans and radiology reports. We also curate the first dataset for 3D medical VLP from public sources enable T3D to surpass SOTA vSSL baselines in various 3D medical imaging tasks. We believe that T3D and the BIMCV-VLP dataset will significantly contribute to future explorations in the 3D medical VLP domain.

References

- [1] Michela Antonelli, Annika Reinke, Spyridon Bakas, Keyvan Farahani, Annette Kopp-Schneider, Bennett A Landman, Geert Litjens, Bjoern Menze, Olaf Ronneberger, Ronald M Summers, et al. The medical segmentation decathlon. *Nature communications*, 13(1):4128, 2022. 5, 6
- [2] Spyridon Bakas, Mauricio Reyes, Andras Jakab, Stefan Bauer, Markus Rempfler, Alessandro Crimi, Russell Takeshi Shinohara, Christoph Berger, Sung Min Ha, Martin Rozycki, et al. Identifying the best machine learning algorithms for brain tumor segmentation, progression assessment, and overall survival prediction in the brats challenge. *arXiv preprint arXiv:1811.02629*, 2018. 6

	Brain Tumour	Lung Tumour
w Report	87.7±4.0	63.6±4.1
w/o Report	85.2±5.3	57.8±7.5

(a) Ablation of the Report. ‘w/o Report’ denotes attention solely applied to visual features in the interactor.

	Brain Tumour	Lung Tumour
ClinicalBERT [17]	87.3±4.1	63.4±4.5
RadBERT [4]	87.7±4.0	63.6±4.1

(b) Affect of Text Encoder.

Backbone	Brain Tumour	Lung Tumour
U-Net [32]	87.4±4.3	64.1±4.6
SwinUNTER [34]	87.7±4.0	63.6±4.1

(c) Ablation of Backbone

Number of Heads	Brain Tumour	Lung Tumour
1	86.5±5.2	62.7±4.4
2	87.7±4.0	63.6±4.1
3	87.1±4.0	63.2±5.3
4	87.2±5.0	63.0±5.1

(d) Number of attention heads in Interactor

	Brain Tumour	Lung Tumour
w/o \mathcal{L}_{TIR}	85.2±5.5	61.4±5.1
w/o \mathcal{L}_{TCL}	84.4±4.9	61.9±4.7
Ours	87.7±4.0	63.6±4.1

(e) Loss Ablation

Transformer Layers	Brain Tumour	Lung Tumour
1	87.7±4.0	63.6±4.1
2	86.9±4.5	63.1±4.6
3	87.2±4.3	63.3±5.2

(f) Ablation of Transformer Layers in Interactor

Table 7. Results of various ablation experiments. The best results are bolded.

- [3] Krishna Chaitanya, Ertunc Erdil, Neerav Karani, and Ender Konukoglu. Contrastive learning of global and local features for medical image segmentation with limited annotations. *Advances in neural information processing systems*, 33:12546–12558, 2020. 1, 3
- [4] Pierre Chambon, Tessa S Cook, and Curtis P Langlotz. Improved fine-tuning of in-domain transformer model for inferring covid-19 presence in multi-institutional radiology reports. *Journal of Digital Imaging*, 36(1):164–177, 2023. 6, 8, 9, 12
- [5] Liang Chen, Paul Bentley, Kensaku Mori, Kazunari Misawa, Michitaka Fujiwara, and Daniel Rueckert. Self-supervised learning for medical image analysis using image context restoration. *Medical image analysis*, 58:101539, 2019. 3, 6, 7
- [6] Mark Chen, Alec Radford, Rewon Child, Jeffrey Wu, Heewoo Jun, David Luan, and Ilya Sutskever. Generative pre-training from pixels. In *International conference on machine learning*, pages 1691–1703. PMLR, 2020. 1, 3
- [7] Qiuhui Chen, Xinyue Hu, Zirui Wang, and Yi Hong. Medblip: Bootstrapping language-image pre-training from 3d medical images and texts. *arXiv preprint arXiv:2305.10799*, 2023. 3
- [8] Sijin Chen, Hongyuan Zhu, Xin Chen, Yinjie Lei, Gang Yu, and Tao Chen. End-to-end 3d dense captioning with vote2cap-detr. In *Proceedings of the IEEE/CVF Conference on Computer Vision and Pattern Recognition*, pages 11124–11133, 2023. 3
- [9] Yinda Chen, Che Liu, Wei Huang, Sibao Cheng, Rossella Arcucci, and Zhiwei Xiong. Generative text-guided 3d vision-language pretraining for unified medical image segmentation. *arXiv preprint arXiv:2306.04811*, 2023. 3
- [10] Zekai Chen, Devansh Agarwal, Kshitij Aggarwal, Wiem Safta, Mariann Micsinai Balan, and Kevin Brown. Masked image modeling advances 3d medical image analysis. In *Proceedings of the IEEE/CVF Winter Conference on Applications of Computer Vision*, pages 1970–1980, 2023. 3, 6, 7
- [11] Pujin Cheng, Li Lin, Junyan Lyu, Yijin Huang, Wenhan Luo, and Xiaoying Tang. Prior: Prototype representation joint learning from medical images and reports. *arXiv preprint arXiv:2307.12577*, 2023. 2
- [12] Spyros Gidaris, Praveer Singh, and Nikos Komodakis. Un-supervised representation learning by predicting image rotations. *arXiv preprint arXiv:1803.07728*, 2018. 1, 3
- [13] Mikhail Goncharov, Vera Soboleva, Anvar Kurmukov, Maxim PISOV, and Mikhail Belyaev. vox2vec: A framework for self-supervised contrastive learning of voxel-level representations in medical images. *arXiv preprint arXiv:2307.14725*, 2023. 2, 3, 5, 6, 7, 8
- [14] Fatemeh Haghighi, Mohammad Reza Hosseinzadeh Taher, Michael B Gotway, and Jianming Liang. Dira: Discriminative, restorative, and adversarial learning for self-supervised medical image analysis. In *Proceedings of the IEEE/CVF Conference on Computer Vision and Pattern Recognition*, pages 20824–20834, 2022. 1, 2, 3
- [15] Kaiming He, Xinlei Chen, Saining Xie, Yanghao Li, Piotr Dollár, and Ross Girshick. Masked autoencoders are scalable vision learners. In *Proceedings of the IEEE/CVF conference on computer vision and pattern recognition*, pages 16000–16009, 2022. 1, 3
- [16] Gregory Holste, Song Wang, Ziyu Jiang, Thomas C Shen, George Shih, Ronald M Summers, Yifan Peng, and Zhangyang Wang. Long-tailed classification of thorax diseases on chest x-ray: A new benchmark study. In *MICCAI Workshop on Data Augmentation, Labelling, and Imperfections*, pages 22–32. Springer, 2022. 12
- [17] Kexin Huang, Jaan Altosaar, and Rajesh Ranganath. Clinicalbert: Modeling clinical notes and predicting hospital readmission. *arXiv preprint arXiv:1904.05342*, 2019. 8, 9
- [18] Shih-Cheng Huang, Liyue Shen, Matthew P Lungren, and Serena Yeung. Gloria: A multimodal global-local representation learning framework for label-efficient medical image recognition. In *Proceedings of the IEEE/CVF International Conference on Computer Vision*, pages 3942–3951, 2021. 2
- [19] Weijian Huang, Hongyu Zhou, Cheng Li, Hao Yang, Jiarun Liu, and Shanshan Wang. Enhancing representation in radiography-reports foundation model: A granular alignment algorithm using masked contrastive learning. *arXiv preprint arXiv:2309.05904*, 2023. 2
- [20] Jaehyup Jeong, Bosoung Jeoun, Yeonju Park, and Bohyung Han. An optimized ensemble framework for multi-label classification on long-tailed chest x-ray data. In *Proceedings of the IEEE/CVF International Conference on Computer Vision*, pages 2739–2746, 2023. 12

- [21] Yankai Jiang, Mingze Sun, Heng Guo, Ke Yan, Le Lu, and Minfeng Xu. Anatomical invariance modeling and semantic alignment for self-supervised learning in 3d medical image segmentation. *arXiv preprint arXiv:2302.05615*, 2023. [1](#), [2](#), [3](#), [12](#)
- [22] Bennett Landman, Zhoubing Xu, J Igelsias, Martin Styner, T Langerak, and Arno Klein. Miccai multi-atlas labeling beyond the cranial vault—workshop and challenge. In *Proc. MICCAI Multi-Atlas Labeling Beyond Cranial Vault—Workshop Challenge*, page 12, 2015. [5](#), [6](#)
- [23] Jiayu Lei, Lisong Dai, Haoyun Jiang, Chaoyi Wu, Xiaoman Zhang, Yao Zhang, Jiagchao Yao, Weidi Xie, Yanyong Zhang, Yuehua Li, et al. Unibrain: Universal brain mri diagnosis with hierarchical knowledge-enhanced pre-training. *arXiv preprint arXiv:2309.06828*, 2023. [2](#), [3](#)
- [24] Che Liu, Sibao Cheng, Chen Chen, Mengyun Qiao, Weitong Zhang, Anand Shah, Wenjia Bai, and Rossella Arcucci. M-flag: Medical vision-language pre-training with frozen language models and latent space geometry optimization. In *International Conference on Medical Image Computing and Computer-Assisted Intervention*, pages 637–647. Springer, 2023. [2](#)
- [25] Che Liu, Sibao Cheng, Miaoqing Shi, Anand Shah, Wenjia Bai, and Rossella Arcucci. Imitate: Clinical prior guided hierarchical vision-language pre-training. *arXiv preprint arXiv:2310.07355*, 2023. [2](#)
- [26] Che Liu, Anand Shah, Wenjia Bai, and Rossella Arcucci. Utilizing synthetic data for medical vision-language pre-training: Bypassing the need for real images. *arXiv preprint arXiv:2310.07027*, 2023. [2](#)
- [27] Yuan Liu, Songyang Zhang, Jiacheng Chen, Kai Chen, and Dahua Lin. Pixmim: Rethinking pixel reconstruction in masked image modeling. *arXiv preprint arXiv:2303.02416*, 2023. [1](#), [3](#)
- [28] Yuan Liu, Songyang Zhang, Jiacheng Chen, Zhaohui Yu, Kai Chen, and Dahua Lin. Improving pixel-based mim by reducing wasted modeling capability. In *Proceedings of the IEEE/CVF International Conference on Computer Vision*, pages 5361–5372, 2023. [1](#), [3](#)
- [29] Deepak Pathak, Philipp Krahenbuhl, Jeff Donahue, Trevor Darrell, and Alexei A Efros. Context encoders: Feature learning by inpainting. In *Proceedings of the IEEE conference on computer vision and pattern recognition*, pages 2536–2544, 2016. [1](#), [3](#)
- [30] Songyou Peng, Kyle Genova, Chiyu Jiang, Andrea Tagliasacchi, Marc Pollefeys, Thomas Funkhouser, et al. Openscene: 3d scene understanding with open vocabularies. In *Proceedings of the IEEE/CVF Conference on Computer Vision and Pattern Recognition*, pages 815–824, 2023. [3](#)
- [31] Alec Radford, Jong Wook Kim, Chris Hallacy, Aditya Ramesh, Gabriel Goh, Sandhini Agarwal, Girish Sastry, Amanda Askell, Pamela Mishkin, Jack Clark, et al. Learning transferable visual models from natural language supervision. In *International conference on machine learning*, pages 8748–8763. PMLR, 2021. [2](#), [4](#), [7](#)
- [32] Olaf Ronneberger, Philipp Fischer, and Thomas Brox. U-net: Convolutional networks for biomedical image segmentation. In *Medical Image Computing and Computer-Assisted Intervention—MICCAI 2015: 18th International Conference, Munich, Germany, October 5-9, 2015, Proceedings, Part III 18*, pages 234–241. Springer, 2015. [8](#), [9](#)
- [33] Aiham Taleb, Winfried Loetzsch, Noel Danz, Julius Severin, Thomas Gaertner, Benjamin Bergner, and Christoph Lippert. 3d self-supervised methods for medical imaging. *Advances in neural information processing systems*, 33:18158–18172, 2020. [1](#), [3](#)
- [34] Yucheng Tang, Dong Yang, Wenqi Li, Holger R Roth, Bennett Landman, Daguang Xu, Vishwesh Nath, and Ali Hatamizadeh. Self-supervised pre-training of swin transformers for 3d medical image analysis. In *Proceedings of the IEEE/CVF Conference on Computer Vision and Pattern Recognition*, pages 20730–20740, 2022. [2](#), [3](#), [5](#), [6](#), [7](#), [8](#), [9](#), [12](#)
- [35] Maria De La Iglesia Vayá, Jose Manuel Saborit, Joaquim Angel Montell, Antonio Pertusa, Aurelia Bustos, Miguel Cazorla, Joaquin Galant, Xavier Barber, Domingo Orozco-Beltrán, Francisco García-García, et al. Bimcv covid-19+: a large annotated dataset of rx and ct images from covid-19 patients. *arXiv preprint arXiv:2006.01174*, 2020. [5](#)
- [36] Pascal Vincent, Hugo Larochelle, Isabelle Lajoie, Yoshua Bengio, Pierre-Antoine Manzagol, and Léon Bottou. Stacked denoising autoencoders: Learning useful representations in a deep network with a local denoising criterion. *Journal of machine learning research*, 11(12), 2010. [1](#), [3](#)
- [37] Zhongwei Wan, Che Liu, Mi Zhang, Jie Fu, Benyou Wang, Sibao Cheng, Lei Ma, César Quilodrán-Casas, and Rossella Arcucci. Med-unic: Unifying cross-lingual medical vision-language pre-training by diminishing bias. *arXiv preprint arXiv:2305.19894*, 2023. [2](#), [6](#), [12](#)
- [38] Fuying Wang, Yuyin Zhou, Shujun Wang, Varut Vardhanabhuti, and Lequan Yu. Multi-granularity cross-modal alignment for generalized medical visual representation learning. *arXiv preprint arXiv:2210.06044*, 2022. [2](#)
- [39] Hongyi Wang, Lanfen Lin, Hongjie Hu, Qingqing Chen, Yinhao Li, Yutaro Iwamoto, Xian-Hua Han, Yen-Wei Chen, and Ruofeng Tong. Patch-free 3d medical image segmentation driven by super-resolution technique and self-supervised guidance. In *Medical Image Computing and Computer Assisted Intervention—MICCAI 2021: 24th International Conference, Strasbourg, France, September 27–October 1, 2021, Proceedings, Part I 24*, pages 131–141. Springer, 2021. [2](#)
- [40] Hongyi Wang, Yingying Xu, Qingqing Chen, Ruofeng Tong, Yen-Wei Chen, Hongjie Hu, and Lanfen Lin. Adaptive decomposition and shared weight volumetric transformer blocks for efficient patch-free 3d medical image segmentation. *IEEE Journal of Biomedical and Health Informatics*, 2023. [2](#)
- [41] Chen Wei, Haoqi Fan, Saining Xie, Chao-Yuan Wu, Alan Yuille, and Christoph Feichtenhofer. Masked feature prediction for self-supervised visual pre-training. In *Proceedings of the IEEE/CVF Conference on Computer Vision and Pattern Recognition*, pages 14668–14678, 2022. [1](#), [3](#)
- [42] Chaoyi Wu, Xiaoman Zhang, Ya Zhang, Yanfeng Wang, and Weidi Xie. Medklip: Medical knowledge enhanced language-image pre-training for x-ray diagnosis. In *Proceed-*

- ings of the *IEEE/CVF International Conference on Computer Vision (ICCV)*, pages 21372–21383, 2023. [2](#)
- [43] Chaoyi Wu, Xiaoman Zhang, Ya Zhang, Yanfeng Wang, and Weidi Xie. Towards generalist foundation model for radiology. *arXiv preprint arXiv:2308.02463*, 2023. [2](#), [3](#)
- [44] Yutong Xie, Jianpeng Zhang, Yong Xia, and Qi Wu. Unimiss: Universal medical self-supervised learning via breaking dimensionality barrier. In *European Conference on Computer Vision*, pages 558–575. Springer, 2022. [1](#), [2](#), [3](#)
- [45] Zhenda Xie, Zheng Zhang, Yue Cao, Yutong Lin, Jianmin Bao, Zhuliang Yao, Qi Dai, and Han Hu. Simmim: A simple framework for masked image modeling. In *Proceedings of the IEEE/CVF Conference on Computer Vision and Pattern Recognition*, pages 9653–9663, 2022. [1](#), [3](#)
- [46] Le Xue, Mingfei Gao, Chen Xing, Roberto Martín-Martín, Jiajun Wu, Caiming Xiong, Ran Xu, Juan Carlos Niebles, and Silvio Savarese. Ulip: Learning a unified representation of language, images, and point clouds for 3d understanding. In *Proceedings of the IEEE/CVF Conference on Computer Vision and Pattern Recognition*, pages 1179–1189, 2023. [3](#)
- [47] Le Xue, Ning Yu, Shu Zhang, Junnan Li, Roberto Martín-Martín, Jiajun Wu, Caiming Xiong, Ran Xu, Juan Carlos Niebles, and Silvio Savarese. Ulip-2: Towards scalable multimodal pre-training for 3d understanding. *arXiv preprint arXiv:2305.08275*, 2023.
- [48] Yihan Zeng, Chenhan Jiang, Jiageng Mao, Jianhua Han, Chaoqiang Ye, Qingqiu Huang, Dit-Yan Yeung, Zhen Yang, Xiaodan Liang, and Hang Xu. Clip2: Contrastive language-image-point pretraining from real-world point cloud data. In *Proceedings of the IEEE/CVF Conference on Computer Vision and Pattern Recognition*, pages 15244–15253, 2023. [3](#)
- [49] Xiaoman Zhang, Chaoyi Wu, Ya Zhang, Weidi Xie, and Yanfeng Wang. Knowledge-enhanced visual-language pre-training on chest radiology images. *Nature Communications*, 14(1):4542, 2023. [2](#)
- [50] Yuhao Zhang, Hang Jiang, Yasuhide Miura, Christopher D Manning, and Curtis P Langlotz. Contrastive learning of medical visual representations from paired images and text. *arXiv preprint arXiv:2010.00747*, 2020. [2](#)
- [51] Hong-Yu Zhou, Chenyu Lian, Liansheng Wang, and Yizhou Yu. Advancing radiograph representation learning with masked record modeling. In *The Eleventh International Conference on Learning Representations*. [2](#)
- [52] Hong-Yu Zhou, Chixiang Lu, Chaoqi Chen, Sibe Yang, and Yizhou Yu. A unified visual information preservation framework for self-supervised pre-training in medical image analysis. *IEEE Transactions on Pattern Analysis and Machine Intelligence*, 2023. [2](#), [3](#), [6](#), [7](#), [12](#)
- [53] Lei Zhou, Huidong Liu, Joseph Bae, Junjun He, Dimitris Samaras, and Prateek Prasanna. Self pre-training with masked autoencoders for medical image classification and segmentation. *arXiv preprint arXiv:2203.05573*, 2022. [3](#), [6](#), [7](#)
- [54] Zongwei Zhou, Vatsal Sodha, Md Mahfuzur Rahman Siddiquee, Ruibin Feng, Nima Tajbakhsh, Michael B Gotway, and Jianming Liang. Models genesis: Generic autodidactic models for 3d medical image analysis. In *Medical Image Computing and Computer Assisted Intervention—MICCAI 2019: 22nd International Conference, Shenzhen, China, October 13–17, 2019, Proceedings, Part IV 22*, pages 384–393. Springer, 2019. [3](#), [6](#), [7](#)
- [55] Jia-Xin Zhuang, Luyang Luo, and Hao Chen. Advancing volumetric medical image segmentation via global-local masked autoencoder. *arXiv preprint arXiv:2306.08913*, 2023. [3](#)

Appendix

Pre-training Implementation Details

During pre-training, we further fine-tune the language model, RadBERT [4], using the Masked Language Modeling (MLM) task to enable the text encoder to tokenize and understand the Spanish corpus. The MLM configuration is inherited from [37]. For data preprocessing and augmentation, we strictly follow the protocol from SwinUNTER [34]. For other baselines, we reimplement them according to their official code on the BIMCV-VLP dataset. We provide a more detailed distribution visualization of the pre-training dataset BIMCV-VLP in Fig 5.

Downstream Tasks Implementation Details

Multi-organ Segmentation

In this task, all CT scans are interpolated to achieve an isotropic voxel spacing of $[1.5 \times 1.5 \times 2.0]$ mm. The multi-organ segmentation problem is tackled as a 13-class segmentation task, encompassing large organs such as the liver, spleen, kidneys, and stomach; vascular tissues including the esophagus, aorta, IVC, splenic, and portal veins; as well as smaller anatomies like the gallbladder, pancreas, and adrenal glands. A soft tissue window is employed for clipping the CT intensities, which are then normalized to a range of 0 to 1. Subsequently, random samples of $96 \times 96 \times 96$ voxels are generated. Data augmentation techniques such as random flipping, rotation, and intensity shifting are employed during training, with respective probabilities of 0.1, 0.1, and 0.5. All training configurations are based on the publicly available SwinUNETR [34] codebase, accessible at: <https://github.com/Project-MONAI/research-contributions/tree/main/SwinUNETR/BTCV>

Lung Tumor Segmentation

In this task, each image is interpolated to achieve an isotropic voxel spacing of 1.0. The Hounsfield Unit (HU) range is set between $[-1000, 1000]$ and is subsequently normalized to the range $[0, 1]$. For the training phase, samples are cropped to dimensions of $96 \times 96 \times 96$, maintaining a positive to negative ratio of 2 : 1. Augmentation techniques are applied with probabilities of 0.5, 0.3, 0.1, and 0.1 for random flipping, rotation, intensity scaling, and shifting, respectively. All the training configurations are derived from the publicly accessible SwinUNETR [34] codebase, which can be found at: <https://github.com/Project-MONAI/research-contributions/tree/main/SwinUNETR/BTCV>

https://github.com/Project-MONAI/research-contributions/blob/main/SwinUNETR/Pretrain/utis/data_utils.py

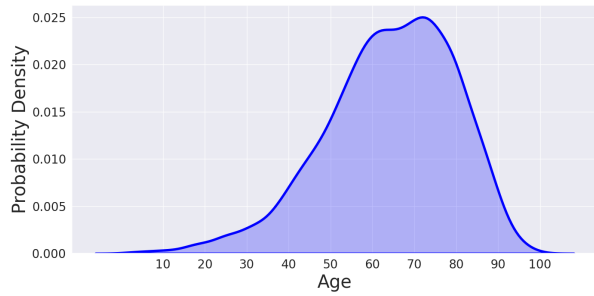
Brain Tumor Segmentation

In this task, AdamW is employed as the default optimizer. The initial learning rate is set to 1×10^{-5} , and a cosine annealing strategy is utilized for managing the learning rate decay, with the weight decay configured to 1×10^{-4} . For fine-tuning, a batch size of 2 is used, and the process is run for 100 epochs across all fine-tuning data ratios. The Dice similarity coefficient is employed as the evaluation metric. Dice loss is utilized for the fine-tuning process. All training configurations are derived from the publicly available PCRLv2 [52] codebase, which can be accessed at: <https://github.com/RL4M/PCRLv2/tree/finetune>

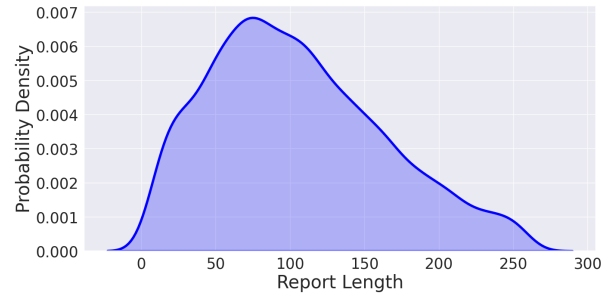
Multi-disease Classification

We conduct this task on the MDLT dataset. As illustrated in Fig 6, the label distribution of the MDLT dataset exhibits a severe long-tail issue. Due to this, we employ the macro-average AUC score as the metric, which is commonly used in long-tail classification tasks [16, 20]. We fine-tune all parameters from the visual encoder of the pre-trained model, along with a randomly initialized linear layer for this task. In accordance with [21], we resize the entire CT volume to match the input dimension used during the pre-training stage, which is $96 \times 96 \times 96$. For data augmentation, we utilize RandCoarseDropout, RandCoarseShuffle, RandFlip, RandRotate90, and RandShiftIntensity, all of which are implemented using MONAI. We employ AdamW as our optimizer for all fine-tuning data ratios. For 1% and 10% data fine-tuning, the batch size is set to 2, the learning rate to $1e-5$, and the weight decay to $1e-8$. For 20% and 100% data fine-tuning, the batch size is set to 8, the learning rate to $2e-5$, and the weight decay remains at $1e-8$. We utilize BCE loss for all fine-tuning data ratios.

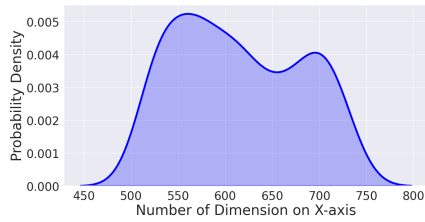
<https://docs.monai.io/en/stable/transforms.html>



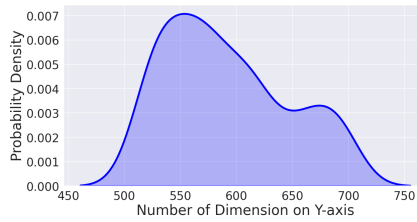
(a) The distribution of participants' ages.



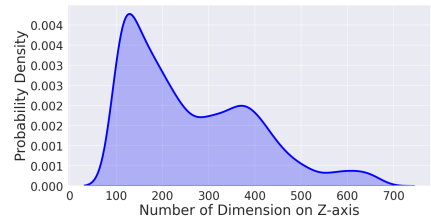
(b) The distribution of report length.



(c) The distribution of the number of image dimensions on the X-axis.



(d) The distribution of the number of image dimensions on the Y-axis.



(e) The distribution of the number of image dimensions on the Z-axis.

Figure 5. Details of the BIMCV-VLP dataset.

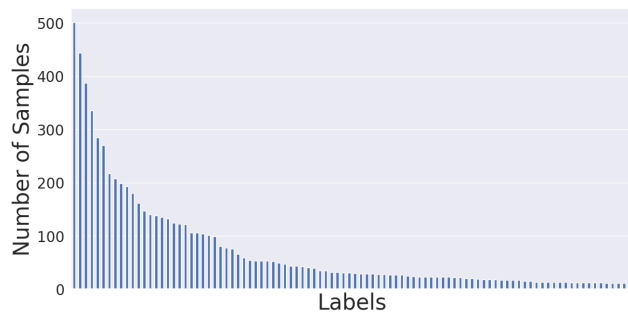


Figure 6. Label distribution in the multi-disease classification dataset.